Available online at www.sciencedirect.com

ScienceDirect

Procedia CIRP 104 (2021) 600–605

www.elsevier.com/locate/procedia

54th CIRP Conference on Manufacturing Systems

Approach to an optimized printing path for additive manufacturing in construction utilizing FEM modeling

Lukas Lachmayer[a,]*, Virama Ekanayaka[b], André Hürkamp[b], Annika Raatz[a]

[a]*Institute of Assembly Technology, Leibniz Universität Hannover, An der Universität 2, 30823 Garbsen, Germany*
[b]*Institute of Machine Tools and Production Technology, Technische Univeristät Braunschweig, Langer Kamp 19b, 38106 Braunschweig, Germany*

* Corresponding author. Tel.: +49-511-762-18278; fax: +49-511-762-18251. *E-mail address:* lachmayer@match.uni-hannover.de

Abstract

Based on experiences with common additive manufacturing processes, the application in the construction industry opens up new design freedoms and cost-effective production of complex structures. However, the time-dependent yield strength of fresh concrete leads to deformations of underlying layers during the printing process, especially when using conventional path planning methods in combination with material extrusion or jetting methods. This paper presents a finite element model based approach to minimize the resulting deviations from the target geometry by iteratively adjusting the process parameters according to simulated deformations. To achieve more detailed modelling, the utilized finite element model is derived from the printing path instead of the CAD data.

Keywords: path planning; path optimization; FEM modeling; additive manufacturing in construction; concrete printing

1. Introduction

Additive manufacturing in construction (AMC) currently presents itself as one of the critical technologies for increasing productivity in the construction industry. In particular, opportunities to reduce production costs, material usage, and physical labor attract a wide range of attention [1,2]. In this respect, the most significant potential is ascribed to eliminating formwork elements, whereby however the time-dependent material properties and the printing path decisively define the buildability of a component [3,4].

For extrusion-based layer-by-layer construction of 3D printed concrete components, the buildability is defined as the number of layers laid on top of each other without the previous layers' failure [5]. Two basic approaches are available to determine the buildability. Classically the number of possible layers estimated based on empirical parameter studies [6-8]. Hence these experimental data must not be extrapolated and has no general validity this costly and time-consuming approach is displaced by more recent methods. These focus on modelling the printing process within finite element analysis (FEA) software. Therefore the material behavior is described based on time-dependent material parameters such as Young's modulus, Possion's ration, cohesion, angle of internal friction, dilatancy angle, and yield stress [9,10].

Although the latter strategy requires a much more complex material investigation and demands more computing effort, it offers the opportunity to generate a simulation of the entire printing process. The latest research programs have shown this approach's suitability in principle and especially point out challenges regarding the model computation time and the exact transformation of the time-dependent extrusion path into the modelling environment [11,12]. Mostly the entire CAD-model is used, which leads to a significant discrepancy between the geometries used for the simulation and the actual printing process [13].

To enhance the modelling performance, this paper presents a new approach to perform a FEA based on the printing path.

10.1016/j.procir.2021.11.101

By successively adding volume to the model and taking into account the time dependent material properties the printing process is simulated as is. Thus, achieving better results from more detailed FEA, the obtained loads and deformations can be used within an additionally proposed feedback loop.

In this regard, the layer width and heights of the printed material are suggested as path optimization parameters to reduce the deviation between CAD model and simulated deformations. Using the optimized printing paths will finally lead to better component quality, reduced test effort, and fewer buildability failures.

1.1. Path planning for additive manufacturing in construction

Concrete 3D printing is explicitly limited by the stability of the fresh concrete and the time-dependent flow behavior. Especially the latter leads to restrictions in the design of overhangs and is influencing the interlayer strength. Both effects limit the printable geometries' freedom, so in contrast to other additive manufacturing techniques, the predominant research for path planning concepts for concrete components with multiple layers is still based on 2.5D approaches with planar slicing [14,15].

The base element for most of those 2.5D printing processes is the target objects' outer contour, which is used to generate a shell structure. In the next step, the shell's wall thickness will be increased to the necessary stability level by applying one or more additional parallel strands with an inward offset [16,17].

Within each layer, an infill will further extend the contour path to generate additional stability and prevent buildability failures. Therefore, multiple continuous infill patterns have been developed and rated according to buildability improvement. Varying the infill density by refining the chosen infill pattern also improves the final component's overall stability and has been used to control the result [18,19]. While many different approaches are available and some even take into account multiple planning criteria [20], there is still a lack of consolidation within a generally valid procedure. However, general boundary conditions can be derived from the investigated path planning concepts, which will be recapitulated subsequently.

Interrupting the material flow will foster the fresh concrete to cure within the conveyor pump, the hoses, and the extrusion nozzle when the printing process must be stopped. Therefore all path planning concepts have in common that the final path provides a continuous material application. This continuity is of utmost interest for all upcoming development to prevent clocking and ensure a successful printing process. Besides, overlaps within one layer are avoided in order to ensure a uniform application height. Both aspects are further set as strict constraints for the path planning algorithm.

As an extension to existing path planning methods, the path coordinates derived in this paper will provide the input for a FEA, which allows observing the material flow during the printing process. Further processing resulting simulation data will lead to an improved component quality when minimizing the observed deformations by adapting the printing path and parameters.

1.2. Finite element analysis for additive manufacturing

The prediction of deformation and residual stress of a structure is essential in determining its mechanical properties. Especially in structures constructed through additive manufacturing, as they are prone to thermally or mechanically induced residual stresses and distortions, this consideration is crucial. Therefore, in FEA of structures constructed through additive manufacturing, the material application process is simulated.

As opposed to a standard structural FEA where the deformations and stresses of a fixed input geometry are calculated, in additive manufacturing the input geometry itself is changing with time as new layers are added on top of the existing layers to construct the structure. This adds an additional layer of complexity to the FEA. The ultimate goal of FEA in additive manufacturing is adjusting the printing parameters for achieving the desired mechanical integrity, reducing the formation of structural failures and towards minimizing manufacturing costs [21].

Current approaches capable of performing stress and deformation analysis of structures manufactured using AM techniques [21,22]. The CAD model (target geometry) of the structure to be printed, the printing speed and material deposition thickness are among the inputs used in FEA by commercial software. The complete CAD model is initially meshed, and a subset of this mesh is simulated with time to calculate the resulting deformations, as the structure is constructed layer wise. In order to determine which subset of the mesh should be simulated at a given time, the toolpath is used. All elements that have intersected with the toolpath at a given time step are then activated and simulated.

The G-Code, which contains the toolpath information, together with the target CAD model can be used to carry out an FEA in additive manufacturing. The G-Code contains the printing information required for 3D printing such as the toolpath, feed rate, etc. The G-Code is used to determine which elements in the mesh of the target CAD model are active at a given time step [22].

The disadvantage of such an approach is that the target geometry is used for the analysis. The approach, which utilizes the G-Code, does not create the printed geometry and instead only determines the active elements of the target geometry. However, depending on the printing path, the printed geometry would have deviations from the target geometry even before deformation due to stress are considered. Utilizing the nodal displacements computed by the FEA model, the deviation between the printed geometry and the target geometry can be reduced through suitable adjustments of the nozzle velocity and path point coordinates.

2. Contour-Offset based path planning

Initially, a contour-offset-based path-planning algorithm was implemented in MATLAB to be used as the resulting waypoint representation of the toolpath. This waypoint representation is used as the input to the FEA. According to section 1.1, a continuous printing path without overlapping was aimed for. Since stereolithography files are the most used

representation of 3D geometries, the algorithm was developed to take the STL as input. Additionally to the desired geometry, the layer height L_h and the minimal path width $L_{b,min}$, are required to generate the toolpath.

Based on the constant layer height L_h evenly distanced cross-sections are calculated along the vertical direction, utilizing a uniform-slicing approach. The contours of the cross-sections have varying widths, which dictates that the printing path's starting point must not lay within the contour's narrowest part in order to prevent overlapping and ensure a continuous path. For the double-curved freeform wall in Fig. 1.a, a simple offset-based printing path would lead to the overlap error marked in Fig. 1.b.

The following algorithm's main idea is to define an initial path point within that narrowest part and then follow the contour left and right until an overlap occurs, as shown in Fig. 1.c. The narrowest part of the contour corresponds to the region where the offset points are clustered closest to each other. Then through following the offset curve from the defined start point via the initial point to the end point would provide the longest possible printing path without an overlap. The determination of the initial point is conducted by utilizing a point representation of the offset curve and the distances between all these offset points. The offset value is set to $L_{b,min}/2$.

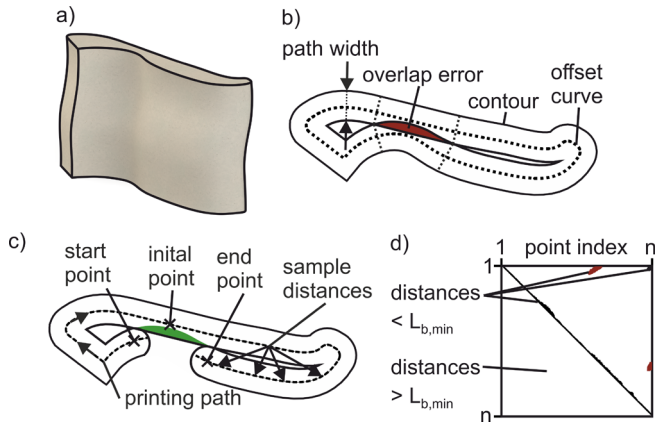

Fig. 1. (a) Sample wall; (b) Offset printing path; (c) Overlap elimination approach; (d) Distance image for sample layer

According to Fig. 1.d, the calculated distances between all offset points of one layer can be mapped into a 2D image with the x- and y-axis representing the indices of each point. The 2D image is a $n \times n$ matrix, where each entry d_{ij} corresponds to the distance between the offset points i and j. All distances greater than the minimal path width are set to zero and marked in white. Smaller values are replaced by one and appear in black or red. At first, the resulting image will be symmetrical to the main diagonal because, e.g. the distance value from point i to point j will be the same as from point j to point i. Therefore, it is sufficient to consider only the upper right triangular matrix for further calculation, to reduce complexity during image processing. Thus, all entries below the main diagonal are changed to white.

By grouping the remaining areas, two main areas can be extracted for all input geometries. One area always appears close to the main diagonal, and another small one in the upper right corner of the image. Both domains emerge from consequent points on the offset curve as the distances of consequent points will always be $< L_{b,min}$. Due to this, they are of no interest in identifying the overlapping areas. The goal is to identify the closest distance between different path sections, which might result in overlapping. Thus for the example in Fig. 1.d the significant points with a distance lesser than the path width can be found within the red sections on the upper and on the right edge. In this specific case, searching for the minimal distance within these red areas will lead to the narrowest part of the sample layer and hence to the initial point.

To achieve a more general approach, a variety of sample geometries have been tested, and contours with a width close to the minimal path width caused two additional image cases. Additionally to the four sections in Fig. 1.d , a single area can also occur from the distance evaluation. This will happen for all layers with near minimal path width where the offset will form a narrow rectangle, common to all types of bar elements. An example is shown in Fig. 2.a, where the ideal printing path was also identified manually. Furthermore, Fig. 2.b shows the result for a combination of a bar element with a wider section, which will lead to two areas without additional sections.

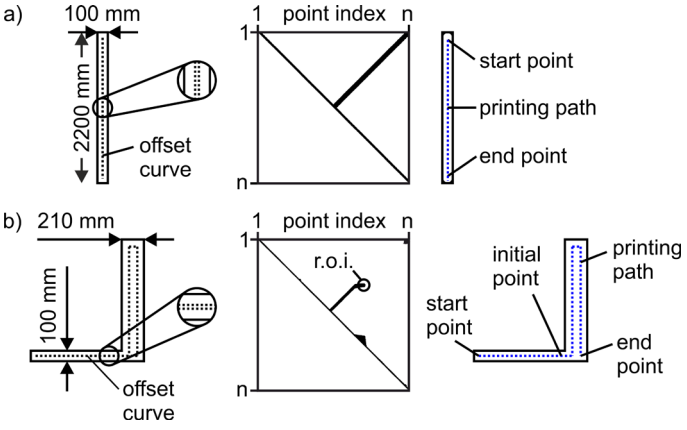

Fig. 2. Test geometries, distance images and ideal printing paths for (a) Layer of a bar; (b) Layer of a L-shaped wall

The selection of the initial point depends on the number of areas in the distance image. If there is one area as in Fig. 2.a, the initial point will be set to the offset curve's first point. When there are two areas as in Fig 2.b, the initial point is chosen from the point coordinates that belong to the region of interest. This region is connected to the main diagonal but has the maximum distance to it. For images with more than two areas as in Fig. 1.d, one of the coordinates with the minimal distance value within the red sections is chosen as the initial point.

After identifying the initial point, the start and end point of the printing path must be set. Therefore, at first, the offset curve points are written in order into a list. This approach will enable using the list of offset points to generate the whole printing path by searching forwards and backwards through the list and identifying the first printing overlaps. Two segments of the offset curve without self-intersection of the printing radius will be found, and the combination of both segments will result in the longest possible continuous path along the contour of the

components. In addition, any overlap will be prohibited, and the given requirements from section 1.1 are met.

Most critical in this procedure is the identification of the stopping points within the forward and backward search. Hence, loops will cause a significant rise in the calculation time when multiple layers have to be processed. This issue is solved by further evaluating the given distance images. The points where a potential overlap will cause a printing failure when moving forward through the list of offset points can be found by observing the distance from the upper edge to the black areas as shown in Fig. 3.a. The first instance at which this distance starts decreasing will mark the start point n_s. When moving backwards through the list, the distance from the right edge to the black areas must be used to get n_e. Fig. 3.b. shows the identified initial point, the forward result n_s, the backward result n_e and the enumeration for the point list to outline the search directions. Looping through multiple layers will generate a path for the whole component consisting of a list of x-, y- and z-coordinates, path width, thickness, and feed rate.

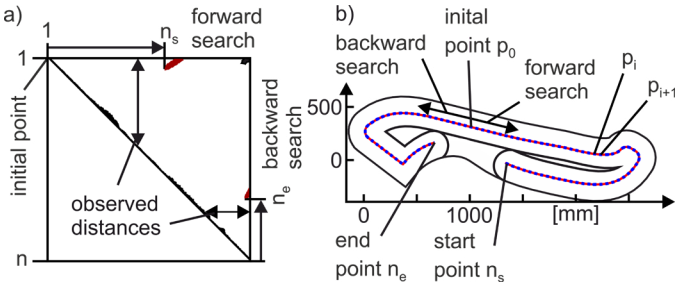

Fig. 3. (a)Search algorithm within the distance image; (b) Search direction for n_s and n_e, and final printing path

3. Path based finite element analysis

Based on the path planning output from section 2 the printing geometry is directly converted into a mesh. At each waypoint $\bar{p}_i$, the material applied from the nozzle is modelled as a circular patch with radius r_i. The mesh geometry is then constructed using the waypoint coordinates and the path thickness, as illustrated in Fig 4, where ds defines the edge length of the elements.

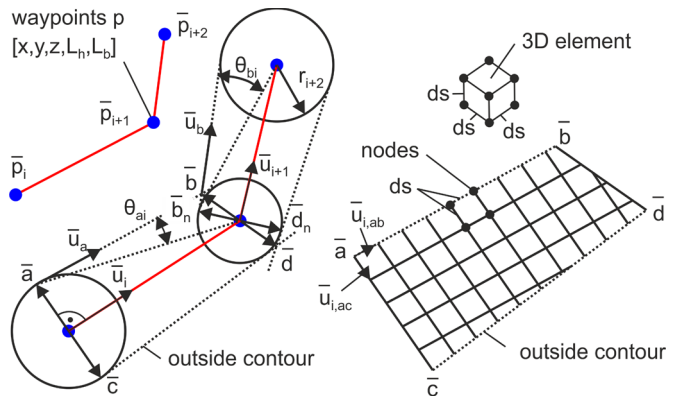

Fig. 4. Waypoint to FEA mesh conversion

At first, the algorithm will create a quadrilateral between two successive path points. This is used to generate a two dimensional mesh, from which the nodes of the finite element model are created by adding the z-coordinate utilizing the specified layer height.

To determine the four vertices $\bar{a}$, $\bar{b}$, $\bar{c}$, and $\bar{d}$ of the quadrilateral shown in Fig. 4, primarily the two-unit vectors $\bar{u}_i$ and $\bar{u}_{i+1}$ are determined according to equation (1) and (2).

$$\bar{u}_i = \frac{\bar{p}_{i+1} - \bar{p}_i}{|\bar{p}_{i+1} - \bar{p}_i|} \tag{1}$$

$$\bar{u}_{i+1} = \frac{\bar{p}_{i+2} - \bar{p}_{i+1}}{|\bar{p}_{i+2} - \bar{p}_{i+1}|} \tag{2}$$

The coordinates of the vertices $\bar{a}$ and $\bar{c}$ are calculated afterwards by rotating $\bar{u}_i$ using the rotation matrix $\bar{R}_z$ and then extending the result by the printing radius r_i.

$$\bar{a} = \bar{p}_i + \bar{R}_z\left(\frac{\pi}{2}\right) \cdot \bar{u}_i \cdot r_i \tag{3}$$

$$\bar{c} = \bar{p}_i + \bar{R}_z\left(-\frac{\pi}{2}\right) * \bar{u}_i * r_i \tag{4}$$

Using path point $\bar{p}_{i+1}$, the unit vector $\bar{u}_{i+1}$ and the printing radius r_{i+1}, the coordinates of the points $\bar{b}_n$ and $\bar{d}_n$

$$\bar{b}_n = \bar{p}_{i+1} + \bar{R}_z\left(\frac{\pi}{2}\right) \cdot \bar{u}_{i+1} \cdot r_{i+1} \tag{5}$$

$$\bar{d}_n = \bar{p}_{i+1} + \bar{R}_z\left(\frac{\pi}{2}\right) \cdot \bar{u}_{i+1} \cdot r_{i+1} \tag{6}$$

are determined, which are then used to compute the last two vertices $\bar{b}$ and $\bar{d}$. The path points $\bar{p}_{i+1}$, $\bar{p}_{i+2}$ and points $\bar{a}$, $\bar{b}_n$ are used to calculate angle θ_{ai} and angle θ_{bi}.

$$\theta_{ai} = \sin^{-1}\left(\frac{r_{i+1}}{|\bar{p}_{i+1} - \bar{a}|}\right) \tag{7}$$

$$\theta_{bi} = \sin^{-1}\left(\frac{r_{i+2}}{|\bar{p}_{i+2} - \bar{b}_n|}\right) \tag{8}$$

$$u_{ai} = \frac{\bar{p}_{i+1} - \bar{a}}{|\bar{p}_{i+1} - \bar{a}|}\,\bar{R}_z(\theta_{ai}) \tag{9}$$

$$u_{bi} = \frac{\bar{p}_{i+2} - \bar{b}_n}{|\bar{p}_{i+2} - \bar{b}_n|}\,\bar{R}_z(\theta_{bi}) \tag{10}$$

It should be noted that the vector u_{ai} will slightly slice through the circumference of the circle with center $\bar{p}_i$. However, this geometric deviation is minimal since the printing radius r_i does not significantly vary between two consequent points and can therefore be neglected. The rotation utilizing the above angles can be used for the computation of the unit vector $\bar{u}_{ai}$ and the unit vector $\bar{u}_{bi}$. In the next step, based on the points $\bar{a}$, $\bar{b}_n$ and the yet unknown scaling magnitudes Δ_a and Δ_b, the

equations (11) and (12) can be derived, both of which computes the point $\bar{b}$.

$$\bar{b} = \bar{a} + \bar{u}_{ai} \cdot \Delta_a \quad (11)$$

$$\bar{b} = \bar{b}_n + \bar{u}_{bi} \cdot \Delta_b \quad (12)$$

By expanding equations (11) and (12), the following linear system of equations (13)

$$\begin{bmatrix} a_x \\ a_y \end{bmatrix} + \begin{bmatrix} u_{ai,x} \\ u_{ai,y} \end{bmatrix} \cdot \Delta_a = \begin{bmatrix} b_{n,x} \\ b_{n,y} \end{bmatrix} + \begin{bmatrix} u_{bi,x} \\ u_{bi,y} \end{bmatrix} \cdot \Delta_b \quad (13)$$

is created, which in turn can be solved to determine the scaling magnitude Δ_a.

$$\Delta_a = \frac{u_{bi,y} \cdot (b_{n,x} - a_x) + u_{bi,x} \cdot (a_y - b_{n,y})}{(u_{ai,x} \cdot u_{bi,y} - u_{bi,x} \cdot u_{ai,y})} \quad (14)$$

The coordinates of the vertice $\bar{b}$ can finally be determined utilizing equation (11). The same procedure is also valid to calculate the coordinates of the vertice $\bar{d}$.In the next step, the two directional unit vectors $\bar{u}_{i,ac}$ and $\bar{u}_{i,ab}$

$$\bar{u}_{i,ac} = \frac{\bar{c} - \bar{a}}{|\bar{c} - \bar{a}|} \quad (15)$$

$$\bar{u}_{i,ab} = \frac{\bar{b} - \bar{a}}{|\bar{b} - \bar{a}|} \quad (16)$$

of the quadrilateral will be calculated. In the final step, the mesh can then be created for all waypoints using the FEM-algorithm shown in Fig. 5. The coordinates of the boundary nodes are computed by utilizing the outside contour. For the tested uniform-slicing algorithm with a constant layer height, the z-coordinates of each element will be set to a specific value determined by the mesh size ds.

Input: CAD-file, material properties
Path planning: points p_1 to p_n
FEM: for *list of all points*
loop
use waypoints $\bar{p}_i$ and $\bar{p}_{i+1}$
n_i = min [$\overline{ab}$, $\overline{cd}$] / ds
n_j = min [$\overline{ac}$, $\overline{bd}$] / ds
for (n_i : n_i-1), (n_j : n_j-1)
calculat each node coordinate
$node_{ij} = \bar{a} + \bar{u}_i \cdot ds \cdot i + \bar{u}_i \cdot ds \cdot j$
$node_{ij,z}$ = [$node_{ij}$(x) $node_{ij}$(y) $node_{ij}$(z)+ds]
end
calculate boundary node coordinates
end
calculate node deformation
Feed back: correct point position and properties
Output: points, layer width, layer heigth

Fig. 5. Meshing algorithm

4. Evaluation of the Finite Element Analysis approach

The described FEA approach was implemented using MATLAB. According to the algorithm shown in Fig. 5 the connectivity between the nodes in the XY-plane was directly determined as the nodes were created. Afterwards the connectivity with the nodes directly above it was calculated in an additional iteration loop.

Fig. 6 shows a section of the printing path illustrated in Fig. 3.b. The points indicated in blue correspond to the individual path points, and the printing path is indicated in red. Three simulation steps of the printing path are shown. The material properties considered in the simulation are the Young's modulus and Poisson's ratio. The model was then simulated stepwise with its own weight as the acting force and under the boundary condition that the bottom-most nodes of the bottom layer were fixed in the Z-direction.

The deformation at each time step is of central interest, as this output from the FEA will be utilized to adapt the printing parameters in order to compensate the computed deformation.

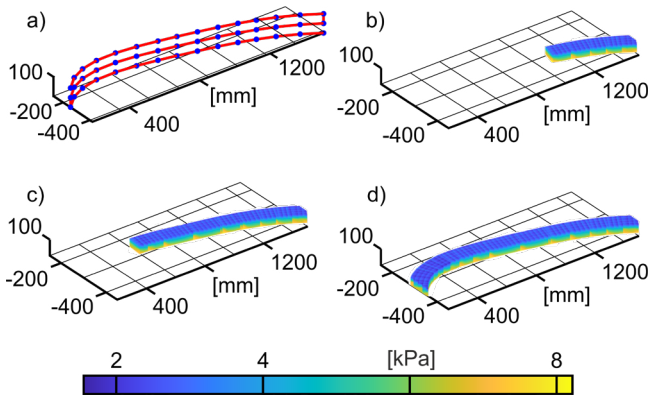

Fig. 6. Path planning a), model building and simulation in MATLAB with time independent material behavior b)-d)

5. Conceptual compensation of geometrical deviations

As shown in Fig. 8 b), lower layers will expand due to the load. Within in the simulation this effect can be measured by the difference between the initial path points and the nearest deformed node, which will lead to $L_{h,diff}$ and $L_{b,diff}$.

To compensate for this deviation, adjustments to the printing parameters are suitable. Thereby changing the nozzle feed rate will directly affect the layer height L_h, when, the concrete flow is constant. Manipulating the distance between the printing nozzle and the printing bed or underlying strand will change the strand width L_b.

Using the calculated differences as an optimization criterion, the values for L_h and L_b will be changed to minimize the absolute deviation between target geometry and the printing result. For the four-layer-wall depicted in Fig. 8. the strand width has to be reduced within the lower layers, and the layer height has to be raised. Since the last layer will not carry any other load, L_b and L_h are set to their initial values. The testing of the feedback loop will be the subject of upcoming research.

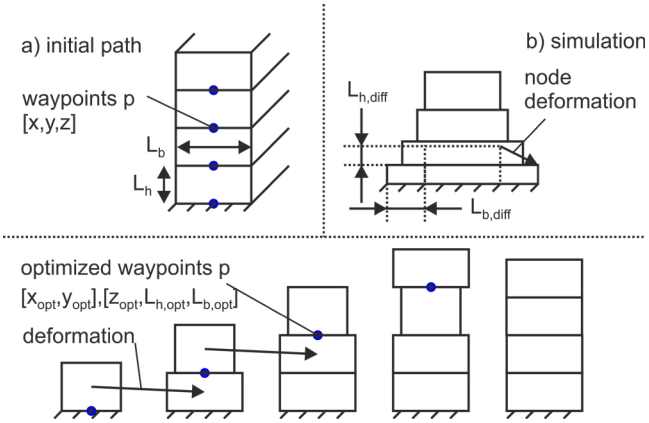

Fig. 7. Printing path optimization based on FEA with (a) initial path, (b) simulated deformation, and its compensation through path adaption

6. Summary and outlook

Additive manufacturing processes currently represent a promising approach to increasing low productivity in the construction industry. However, existing computer-aided control concepts often lead to component failure during the printing process due to the time-dependent flow behavior of fresh concrete. Here, the integration of physical models into the path planning algorithm, and the prediction of the resulting deformations, offers a suitable approach to increase the buildability. This paper provides a contour-based path planning algorithm and the mathematical formulation for generating a FEA model from the path points. The approach was tested in MATLAB with path points generated by the presented algorithm, but in general, can be applied to any printing trajectory. In contrast to common FEA approaches, the described procedure to construct the geometry by directly utilizing the printing path offers the possibility to depict the time-dependent material behavior specifically during the printing process. Furthermore, a methodology is proposed to minimize the predicted deviations of the printed structure from the target geometry by adjusting the path coordinates and the related process parameters.

Acknowledgements

The authors gratefully acknowledge the funding by the Deutsche Forschungsgemeinschaft (DFG – German Research Foundation) – Project no. 414265976. The authors would like to thank the DFG for the support within the SFB/Transregio 277 – Additive manufacturing in construction. (Subproject B04)

References

[1] Bos FP, Wolfs RJM, Amed ZY, Salet TA. M.Additive manufacturing of concrete in construction: potentials and challenges of 3D concrete printing. Virtual and Physical Prototyping; 2016, 11, p. 209-225

[2] Paul SC, Zijl GPAG, Tan MJ, Gibson I. A review of 3D concrete printing systems and materials properties: current status and future research prospects. Rapid Prototyping Journal; 2018, 24, p. 784-798

[3] Tay YWD, Qian Y, Tan MJ. Printability region for 3D concrete printing using slump and slump flow test. Composites Part B; 2019, 174:1359-8368

[4] Dressler I, Freund N, Lowke D. The Effect of Accelerator Dosage on Fresh Concrete and on Interlayer Strength in Shotcrete 3D Printing. Materials; 2020, 13:2-374

[5] Nerella VB, Krause M, Mechtcherine V. Direct printing test for buildability of 3D-printable concrete considering economic viability. Automation in Construction; 2020, 109:0926-5805

[6] Ashrafi N, Nazarian S, Meisel NA, Duarte JP. Experimental Prediction of Material Deformation in Large-Scale Additive Manufacturing of Concrete. Additive Manufacturing; 2021

[7] Kazemian A, Yuan X, Cochran E, Khoshnevis B. Cementitious material for construction-scale 3D printing: Laboratory testing of fresh printing mixture. Construction and Building Materials; 2018, 145, p. 639-647

[8] Bester F, Kruger J, v.d.Hevver M, Zeranka S. Benchmark structures for 3D concrete printing. Proceedings of the fib Symposium; 2019, p. 305-312

[9] Wolfs RJM, Bos FP, Salet TAM. Triaxial compression testing on early age concrete for numerical analysis of 3D concrete printing. Cement and Concrete Composites; 2019, 104:0958-9465

[10] Perrot A, Rangeard D, Pierre A. Structural built-up of cement-based materials used for 3D printing extrusion techniques. Materials and Structures; 2013, 49:1213-1220

[11] Camminal R, Silva WRL, Andersen TJ, Stang H, Spangenber J. Modelling of 3D concrete printing based on computational fluid dynamics. Cement and Concrete Research; 2020, 138:0008-8846

[12] Wolfs RJM, Bos FP, Salet TAM. Early age mechanical behaviour of 3D printed concrete: Numerical modelling and experimental test. Cement and Concrete Research; 2018, 106, p. 103-116

[13] Kahn M., Sanchez F., Zhou H.3-D printing of concrete: Beyond horizons. Cement and Concrete Research; 2020, 133:106070

[14] Buswell RA, Silva WRL, Jones SZ, Dirreenberger J. 3D printing using concrete extrusion: A roadmap for research. Cement and Concrete Research; 2018, 112, p. 37-49

[15] Kontovourkis O, Tryfonos G, Georgiou C. Robotic additive manufacturing with clay using tobology optimization principles for toolpath planning: the example of a building element. Architectural Science Review; 2020, 63, p. 105-118

[16] Grasser G, Pammer L, Köll H, Werner E, Bos FP. Complex architecutre in printed concrete: The case of the Innsbruck University 350th annicaersary pavilion Cohesion. DC 2020 RILEM Bookseries; 2020, 28, p.

[17] Wang Y, Li S, Qin T, Yu Y, Xiao J. Concrete 3D printing: System development, process planning and experimental results. DC 2020 RILEM Bookseries; 2020, 28, p. 998-1010

[18] Douba A, Cha C, Berrios S, Kawashima S. Synthesis of hybridized rehological modifiers for 3D concrete printing. DC 2020 RILEM Bookseries; 2020, 28, p. 32-41

[19] Ibrahim S, Olbrich A, Lindemann H, Gerbers R, Dröder K, Raatz A. Automated Additive Manufacturing of Concrete Structures without Formwork – Concept for Path Planning. Proc. of 3rd MHI Congress; 2018

[20] Papacharalampopoulos A., Bikas H. Foteinopoulos P., Stavropoulos. A Path Planning Optimization Framework for Concrete Based Additive Manufacturing Processes. Procedia Manufacturing; 2020, 51, p. 649-654

[21] Schoinochoritis B, Chantzis D, Salonitis K. Simulation of metallic powder bed additive manufacturing processes with the finite element method: A critical review. Proceedings of the Institution of Mechanical Engineers Part B of Engineering Manufacture; 2015, p. 1-21

[22] Cattenone A, Morganti A, Alaimo G, Auricchio F. Finite element analysis of Additive Manufacturingbased on Fused Deposition Modeling (FDM): distortions prediction and comparison with experimental data. Journal of Manufacturing Science and Engineering; 2019